J Adv Ceram

Research Article

A comprehensive study on flash sintering of anatase and rutile polymorphs-containing titania nanopowder: Phase and microstructure development

Everlin C. F. Silva, Raimundo N. R. Silva, Luís C. Caraschi, Jean-Claude M'Peko✉

Cite this article: Silva ECF, Silva RNR, Caraschi LC, et al. *J Adv Ceram* 2025, **14**(4): 9221062. https://doi.org/10.26599/JAC.2025.9221062

ABSTRACT: Flash sintering has proven to be a novel and cost-efficient technique that enables the successful processing of dissimilar materials. The present work investigated how sintering under electric field input progresses in commercial anatase (A) plus rutile (B) polymorphs containing titania. Both the phase evolution and sintering dynamics were highly dependent on the strength of the field, the application of which led to (A + R) → R → flash at low fields while promoting (A + R) → flash at high fields. A temperature postponement of flash was verified at low fields, as the event was preceded by the A → R transformation, which was responsible for a detectable peak in the thermal spectra of the current. The processing temperature, applied electric field (*E*), and onset flash sintering temperature ($T_{\mathrm{furn}}^{\mathrm{flash}}$) combine well into a phase diagram graph that summarizes the phase development that applies to this material. In addition, high-density bodies in the rutile phase were ultimately produced after flashing under a suitable current density, regardless of the field strength considered. Both the flash sintering temperature and average grain size (AGS) decreased with increasing field. In line with this, we demonstrate the existence of a direct link between the grain size and the sample sintering temperature, which is consistent with the classical grain growth model.

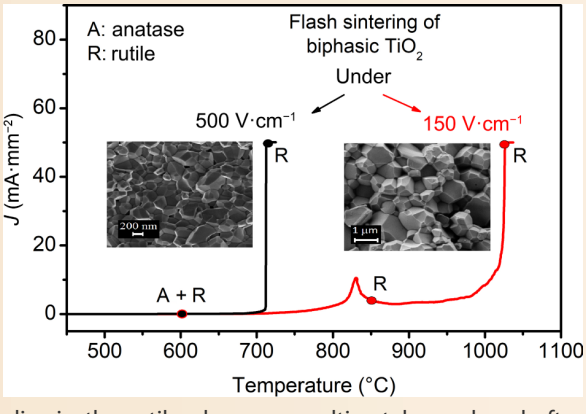

KEYWORDS: titania (TiO_2); flash sintering; current density; phase development; microstructure

1 Introduction

Electrical flash sintering of materials is a novel processing technique that became popular after the work of Cologna *et al.* [1] in 2010. Since then, a variety of simple and complex compounds have been successfully processed, such as doped ZrO_2 [1–5], titania (TiO_2) [6–9], Y_2O_3 [10], $BaTiO_3$ [11], Co_2MnO_4 [12], and $CaCu_3Ti_4O_{12}$ [13,14], to cite a few examples. In all these cases, applying an electric field during heat treatment allows effective sintering of the materials at furnace temperatures lower than those required in the conventional (zero field) approach. The sudden nonlinear increase in the current across the sample and rapid densification are two fingerprints of flash sintering development under field action. In the particular case of TiO_2, which is the material targeted in this work, the influence of different parameters on flash sintering dynamics has been explored, namely, electric field strength [6], doping [7], flash incubation [8], atmosphere [9], etc.

Moreover, reactive flash sintering, in which a multiphase system is converted into a ceramic body via a single-running experimental approach, has also been widely explored, as in Refs. [14–19]. This includes the emblematic case of synthesizing and sintering $CaCu_3Ti_4O_{12}$ (CCTO) starting from an amorphous precursor powder [14–16], which evolved, during thermal processing under field action, to crystallization through intermediate phases, followed by chemical reactions engendering the end single-phase product, plus flash sintering depending on field adjustment [14–16]. This study on CCTO comprised the first-time presentation of field-assisted flash synthesis in Ref. [15]. In another recent case study, the ignition and development of flash sintering in alumina-zirconia mixtures were shown to be dependent on the extent of ion-conducting zirconia within such an insulator–ionic conductor system, with the flashed material ultimately remaining biphasic [20].

In other words, the dynamics of sintering under field input in multiphase systems may vary depending not only on the field strength regulation for a given composite, but also on the involved phases and composition. The present work aimed to explore flash sintering in TiO_2, a material with recognized applicability in photocatalysis, solar cells, varistors, sensor devices, etc. [21–23],

São Carlos Institute of Physics, University of São Paulo (USP), São Carlos 13560-970, Brazil.

✉ Corresponding author. E-mail: peko@ifsc.usp.br

Received: January 23, 2025; Revised: March 10, 2025; Accepted: March 10, 2025

and for which good control of polymorphism evolution is needed. Unlike flash-sintered TiO_2 powder, which was initially a single phase as in Refs. [6–9], here we focus on a commercial TiO_2 nanopowder containing anatase (A) plus rutile (R) polymorphs, namely, TiO_2-P25, which is the most commonly used reference TiO_2 material for studying photocatalytic processes or evaluating the photocatalytic activity of new material [24–26]. The effects of the electric field and current density magnitude on phase development, sintering dynamics, and final microstructural characteristics are presented and discussed, along with an assessment of the electrical transport and grain-boundary migration parameters involved. To the best of our knowledge, flash sintering of mixtures made up of different polymorphs of the same chemical composition has not yet been considered, and two-phase titania is used here as a model material.

2 Experimental

High-purity titania (Aeroxide® TiO_2 P25, Sigma-Aldrich, USA), which was ≥ 99.5% and had a 21 nm primary particle size, was used as the raw material. This powder combines anatase as a major phase and rutile as a minor phase, the composition of which was evaluated, as revealed later. The as-received powder was isostatically cold-pressed into disk-shaped samples at approximately 300 MPa and sintered in the presence of a direct-current (DC) electric field, ranging from $E = 150$ V·cm^{-1} to $E = 500$ V·cm^{-1}, at maximum current densities (J_{max}) preset from 2.5 to 50 mA·mm^{-2}. Platinum electrodes were used at both sample surfaces, and the temperature was increased at a rate of 7 °C·min^{-1}. The thermal behavior of the current flowing across the samples during sintering was monitored via an electrometer (6514, Keithley, USA). For phase development evaluation, the samples were subjected to X-ray diffraction (XRD) measurements at room temperature before and after flashing via a diffractometer (Ultima IV, Rigaku, Japan) operating with Cu Kα (λ = 1.5406 Å) radiation in continuous mode with steps of 0.02° and 2θ varying from 20° to 80°. For comparison purposes, performing some *in situ* XRD measurements while increasing the temperature was also considered, for which a multi-purpose diffractometer (PANalytical X'Pert PRO MPD, PANalytical B.V., the Netherlands) equipped with a high-temperature chamber (Anton Paar HTK 16N, Austria) and a 1.0 mm platinum filament as the heating element was used. This apparatus also operated with Cu Kα radiation in continuous mode, with steps of 0.02° and 2θ varying from 20° to 65°. The measurements were carried out after 10 min of sample annealing at each selected temperature in the 650–1050 °C temperature range. In addition, microstructure examination of the fracture surfaces was performed via a field emission scanning electron microscope (Sigma FEG-SEM, Zeiss, Germany). The samples were fractured and imaged in the cross-section toward the center of their length. The final density of the sintered samples was evaluated via Archimedes' method (using water).

3 Results and discussion

We begin this study by evaluating the phase development dynamics of this biphasic titania nanopowder when subjected to thermal processing under normal conditions, i.e., with no electric field applied ($E = 0$). For this purpose, the nanopowder was heated to, e.g., 600, 830, and 1000 °C, kept there for just 1 min, and then cooled to room temperature, where *ex situ* XRD measurements were subsequently carried out. Figure 1(a) shows the XRD patterns observed, including those collected for the as-received nanopowder. This titania powder originally consisted of anatase (identified with PDF#71-1167) and rutile (PDF#86-147) phases, with the former being the major phase. These patterns reveal that anatase decreases with increasing temperature and, at 1000 °C, the powder is completely in the rutile phase.

Considering that the sintering of materials under field action is usually monitored through *in situ* electrical measurements, we also choose, for the sake of comparison, to perform *in situ* XRD measurements during the thermal processing of this biphasic powder (again with $E = 0$). These results are shown in Fig. 1(b) for the data collected while the powder was annealed at 650, 850, and 1050 °C. The room-temperature pattern of the as-received nanopowder is also included as a reference. As expected, there was a detectable shift in the diffraction peaks toward lower angles as the temperature increased. Regarding relative phase intensities, the observed trends are consistent with the results illustrated in Fig. 1(a). From a quantitative viewpoint, the weight fraction of each phase in titania can be estimated via Spurr and Meyer's equation (Eq. (1)) [27–29]:

$$f_R = \frac{1}{1 + 0.884\left(\frac{I_A}{I_R}\right)} \tag{1}$$

where f_R is the fraction of the rutile phase, and I_A and I_R are the integrated diffraction intensities of the strongest peaks from anatase (101) at 2 $\theta \approx$ 25.2° and rutile (110) at 2 $\theta \approx$ 27.4°, respectively.

The results from applying this equation are presented in Table 1, which shows that the values from the as-received nanopowder are congruent with a previous estimate of the composition of

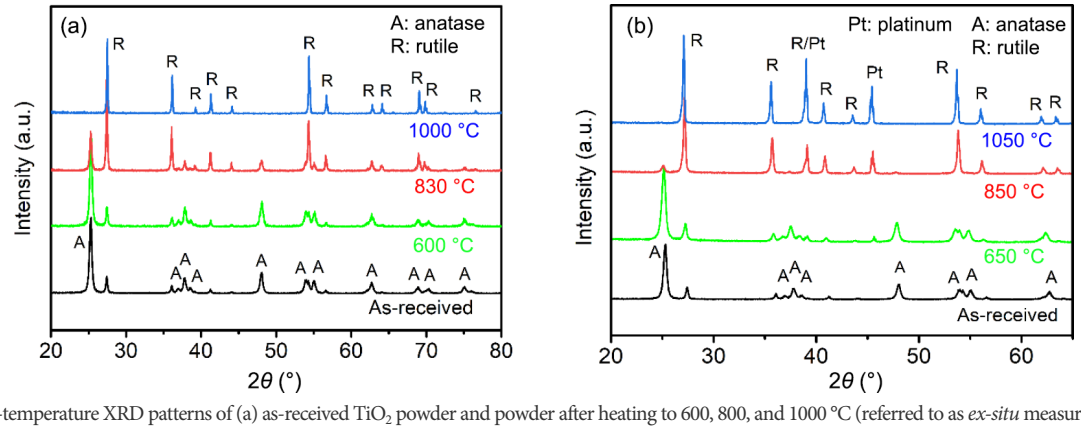

Fig. 1 Room-temperature XRD patterns of (a) as-received TiO_2 powder and powder after heating to 600, 800, and 1000 °C (referred to as *ex-situ* measurements), which were maintained for 1 min, and (b) as-received TiO_2 powder and powder during heat treatment at 650, 850, and 1050 °C (referred to as *in situ* measurements).

Aeroxide TiO_2 P25, e.g., 84.1 wt% for anatase and 15.9 wt% for rutile [30]. All these results, which are taken as reference data to contrast with the results from the flash experiments, allow the conclusion that the A → R phase transformation, known to be of reconstructive type in titania [31], occurs here toward the 600 °C $\leq T \leq$ 900 °C temperature region. Additionally, with respect to conventional processing, 1100 °C was found to be the optimal temperature for sintering this titania powder, with a relative density of 93.5% TD (relative to the theoretical value corresponding to rutile: ρ_R^{theo} = 4.24 g·cm^{-3}), that is, for a holding time of only 2 min.

The results arising from the application of an electric field (E) during the thermal processing of the nanopowder are presented below. Figure 2(a) shows the temperature dependence of the current density (J) measured for processing at E = 150 V·cm^{-1}, with J_{max} preset to 50 mA·mm^{-2}. The data show complex behavior, which includes the occurrence of a current peak at approximately 830 °C and then a sudden, steep increase in current at a given furnace temperature when flash sintering occurs. Similar electrical characteristics were observed for sintering at E = 200 V·cm^{-1} (see below). Meanwhile, the situation was quite different at higher fields ($E \geq$ 300 V·cm^{-1}), toward which the two-phase system progressed to flash without showing any preceding current peak, as revealed in Fig. 2(b) for the sample processed at E = 500 V·cm^{-1} (J_{max} = 50 mA·mm^{-2}). In these experiments, the holding time (t_{flash} = 120 s) at J_{max} was considered. The occurrence of the current peak is addressed later.

The behavior of the current is directly related to that of the electrical conductivity (σ), as $J = \sigma E$. The data depicted in Figs. 2(a) and 2(b) include the behavior of the electric field (E) during thermal processing. As is known in such experiments, when J_{max} is reached at flash, the power supply switches from voltage to current control mode and, in sequence, E decreases to a new value, which is indicative that σ continues to increase for a fleeting time period (transient process) until the system reaches a steady-like state. Figure 3(a) depicts how the power dissipation density ($P \equiv JE$), i.e., Joule heating, across the bodies varied during these experiments. First, the incidence of the current-related peak for $E \leq$ 200 V·cm^{-1} is also registered. Second, as expected, P peaks when J_{max} is reached during flash development. The average values of the onset flash sintering temperature (T_{furn}^{flash}) upon a change in the applied field (i.e., the field before the flash) are summarized in Table 2, but also represented in Fig. 3(b), where open symbols are used, for a better visual assessment of their behavior. These values tend to decrease with increasing E, with a marked change from E = 200 V·cm^{-1}, which represents a type of low-field upper bound (occurrence of the current peak before the flash event), to E = 300 V·cm^{-1}, which is a type of high-field lower bound (no such current peak occurs).

Some comments are here instructive to further portray the electrical scenario found in such flash experiments. For example, the inverse-temperature dependence of the current density (logarithmic scale), as registered for E = 500 V·cm^{-1}, is shown in Fig. 2(b) inset. Three regimes characteristic of the thermal spectra of electrical sintering, namely, linear (I), nonlinear (II), and steady-like (III), are identified. The nonlinear regime includes both the flash incubation region (FIR) and the flash event itself, followed by the steady-like regime that applies during sample holding at J_{max}. Toward the low-temperature linear regime, σ and, thus, J and P are expected to obey Arrhenius-like behaviors (Eq. (2)):

$$P = P_o \exp\left(-\frac{\Delta Q}{kT}\right) \quad (2)$$

where P_o is the pre-exponential factor, ΔQ is the activation energy, k is the Boltzmann constant, and T is the absolute temperature. Accordingly, the low-temperature data in the Arrhenius-type graphs shown in the inset of Fig. 2(b) and Fig. 3(a) are linearized, and the values of the activation energy estimated from these experiments averaged $\Delta Q = (1.5 \pm 0.2)$ eV, in good agreement with energy barrier values also reported elsewhere for the electrical transport in titania [6,32].

From the fundamental viewpoint, claiming a linear regime toward low temperatures presupposes that the relation $J = \sigma E$ should hold, with σ being constant (Ohm's law) at each processing temperature, as verified in Fig. 4. In the linear-scale graph presented in Fig. 4(a), the current data registered for some

Table 1 Estimated values (within an error of approximately 3%) of weight fractions of anatase and rutile in TiO_2-P25 nanopowder after heat treatment at several temperatures, as extracted from *ex situ* and *in situ* XRD measurements (see text for details)

	Phase	As-received	600 °C[&]	650 °C[#]	830 °C[&]	850 °C[#]	1000 °C[&]	1050 °C[#]
TiO_2-P25	A (%)	82.7	80.0	77.6	27.1	14.1	0	0
	R (%)	17.3	20.0	22.4	72.9	85.9	100	100

Note: [&]*ex situ* and [#]*in situ* XRD measurements. The values corresponding to the as-received powder are also included.

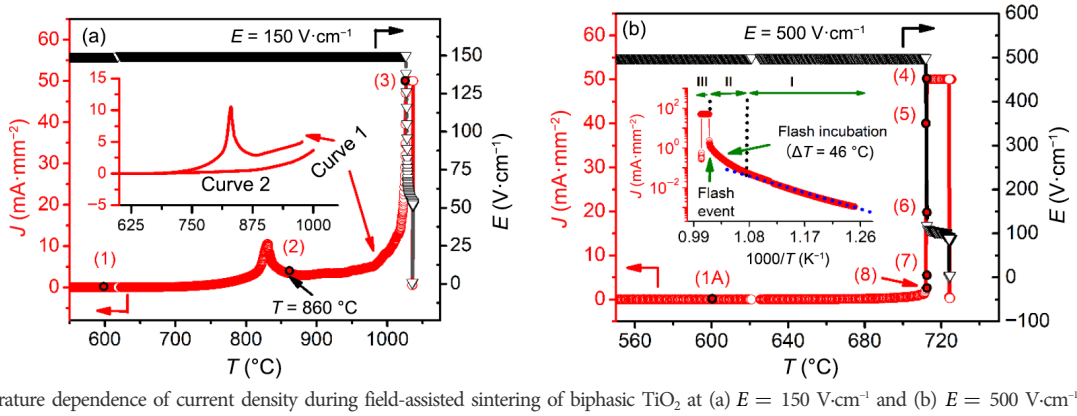

Fig. 2 Temperature dependence of current density during field-assisted sintering of biphasic TiO_2 at (a) E = 150 V·cm^{-1} and (b) E = 500 V·cm^{-1}, with J_{max} = 50 mA·mm^{-2}. Inset in (a) refers to magnification of data around preflash peak (see text for details), whereas inset in (b) refers to an Arrenhius-like graph for current density.

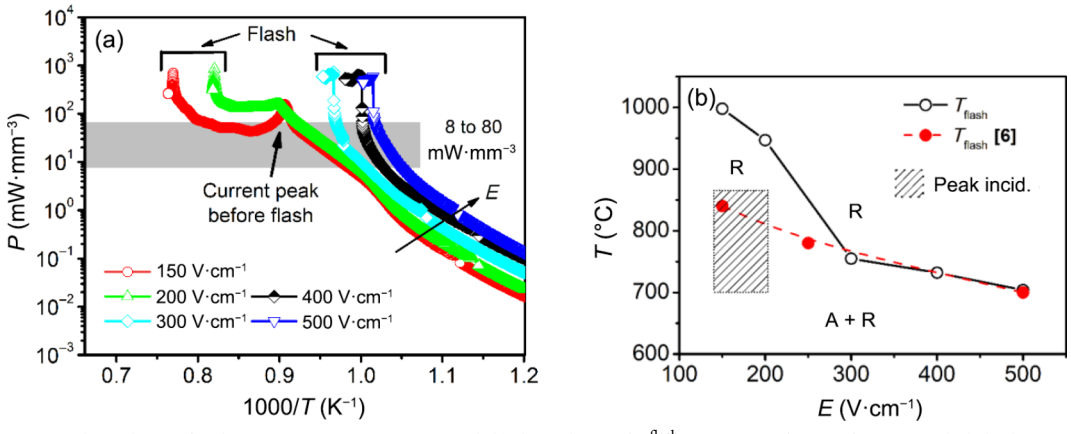

Fig. 3 (a) Temperature dependence of P during sintering experiments and (b) dependence of T_{furn}^{flash} on E. Data from Ref. [6] are included. Phase evolution, with A referring to anatase and R to rutile, has also been specified in (b), making it a phase diagram for this material.

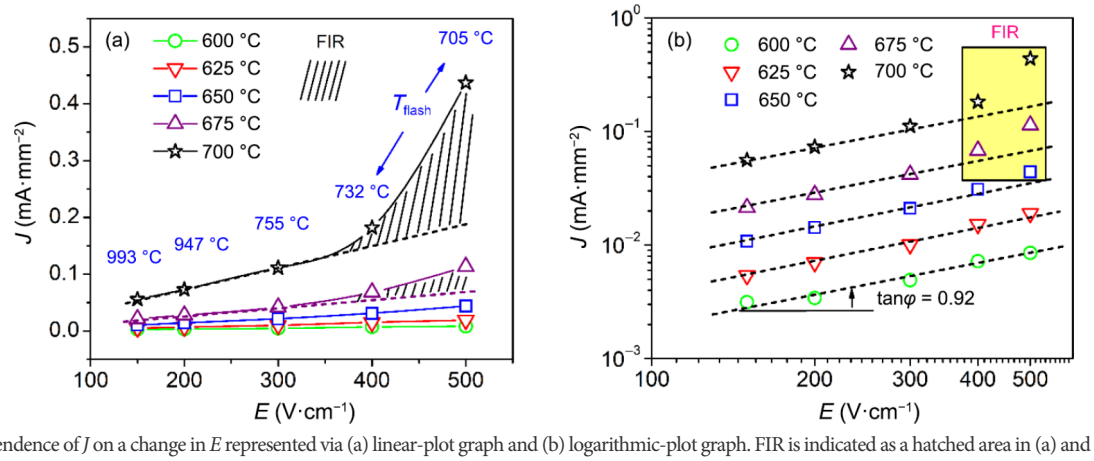

Fig. 4 Dependence of J on a change in E represented via (a) linear-plot graph and (b) logarithmic-plot graph. FIR is indicated as a hatched area in (a) and a box in (b).

representative temperatures (e.g., from 600 to 700 °C) are shown, together with the measured flash onset temperatures (T_{furn}^{flash} going from 705 to 993 °C): these are the values appearing in the vertical line above each corresponding applied electric field. Linear behaviors of J are observed, with the angular coefficient (which is equal to σ in $J = \sigma E$) increasing while raising temperature. In the logarithmic-scale graph illustrated in Fig. 4(b), data linearity is also verified, with the angular coefficients averaging a slope value of 0.92, that is, relatively close to the expected value of unity. In both graphs, divergence from linearity is observed when entering the FIR as the processing temperature approaches T_{furn}^{flash}: the FIR is indicated as the hatched area in Fig. 4(a) and a box in Fig. 4(b).

Returning to Fig. 2, to better understand the complex behavior observed there for the current density (idem for the power dissipation density in Fig. 3), including peak occurrence before flash, the points (1)–(8) are instances where the sintering experiments were stopped, and then XRD measurements were conducted at room temperature. The corresponding diffraction patterns are illustrated in Fig. 5 for the points (1)–(4), including the point (1A). The other points, (5)–(8), will be discussed later. For an approximate evaluation of phase evolution with temperature, refer always to the reference patterns presented in Figs. 1(a) and 1(b), and the extracted quantitative data listed in Table 1. At the points (1) and (1A), related to $E = 150$ and 500 V·cm^{-1}, respectively, both points are located at $T = 600$ °C, and the material is in its original state, that is, it compares well with the cases of the powder as received and that heated to 600 °C (with $E = 0$), all showing both anatase (major) and rutile (minor) phases.

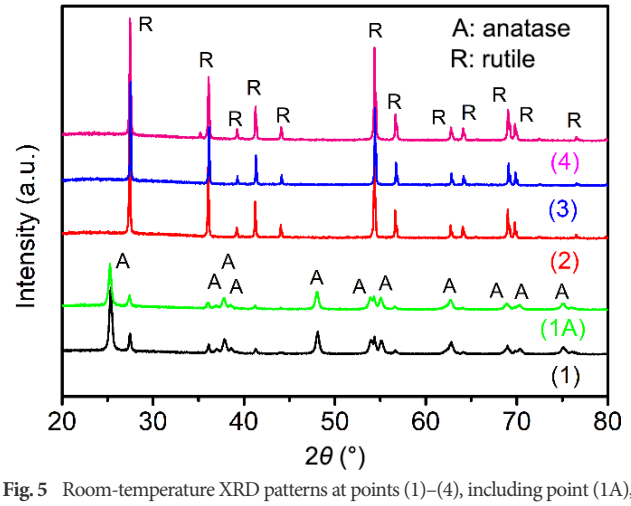

Fig. 5 Room-temperature XRD patterns at points (1)–(4), including point (1A), as indicated in Figs. 2(a) and 2(b), during heating of TiO_2 powder under $E = 150$ and 500 V·cm^{-1}. Points (3) and (4) apply just after preset current density, $J_{max} = 50$ mA·mm^{-2}, is reached, i.e., with no holding time ($t_{flash} = 0$ s).

At the point (2), corresponding to $E = 150$ V·cm^{-1} at $T = 860$ °C, rutile is the only phase detectable, suggesting that the appearance of the anomalous-like current peak in Figs. 2(a) and 3(a) should be related to the A → R transformation. In fact, if the sintering experiment is stopped at point (2) and the same sample is subjected to new heating under field input, starting from a lower temperature, the current peak is no longer observed: this is the

data set identified as curve 2 vs. the original curve 1 in the inset of Fig. 2(a). This particular observation was verified once and again for E =150 and 200 V·cm^{-1}. Finally, at points (3) and (4), i.e., just after J_{max} is reached at flash (t_{flash} =0 s), under E = 150 V·cm^{-1} at T = 1025 °C and E = 500 V·cm^{-1} at T = 712 °C, respectively, only the rutile phase is observed. These results suggest that, for $E \geq$ 300 V·cm^{-1} (where no current peak occurred), the whole system transitions from anatase plus rutile (A + R) to rutile (R) immediately after flash or during the flash incubation or ignition process.

At this point, the question of why the A → R transformation should result in the appearance of a current peak, as verified in Figs. 2(a) and 3(a), is worth addressing. First, the observation of (di)electrical anomalies resulting from phase transformation is indeed not new in the literature. Barium titanate ($BaTiO_3$) is a symbolic case where the dielectric constant (ε', which is the real part of the complex permittivity) and loss ($\tan\delta = \varepsilon''/\varepsilon'$; ε'' is the imaginary part of the complex permittivity) peak at three different phase transition-related temperatures, including at the Curie point (located at approximately 125 °C), when the material's structure transitions from tetragonal ferroelectric to cubic paraelectric upon heating [11,33–35]. The underlying mechanism or source, involving, in that case, polarization-related ferroelectric domain switching and resultant energy dissipation, differs from the titania case presented in this report, as discussed below. In field-assisted processing experiments, the occurrence of preflash current peaks associated with phase development (e.g., crystallization and synthesis) has also been verified elsewhere [14–16].

The finding in the inset of Fig. 2(a) that $J_{curve1} > J_{curve2}$ holds for the current density (J) relation between curves 1 and 2 is equivalent to assuming that anatase is relatively more electrically conductive than rutile, i.e., $J_{anatase} > J_{rutile}$. This is plausible from the perspective of the crystal structure (ionic approach) since the A → R transformation is known to involve a lattice volume contraction of approximately 8% [31]. This means a reduced mobility (μ) for the ionic charge carriers (which are mainly oxygen vacancies in titania, under ordinary conditions [31]) as the free lattice volume for ionic migration [36] undergoes an appreciable drop in rutile. As a consequence, the occurrence of a current anomaly in the temperature region of the A → R transformation is indeed predictable. Moreover, considering that mobility is a thermally activated physical quantity, i.e., $\mu = \mu_o \exp(-\Delta Q/kT)$, and $J\,(\equiv \sigma E) = Nq\mu E$, where N is the density of charge carriers, each with a charge (q), signifying that $J = J_o \exp(-\Delta Q/kT)$, the abovementioned anomaly should manifest as a current peak in the $J - T$ plots, as shown in Fig. 2(a). In the two equations given just above for μ and J, μ_o and J_o refer to the pre-exponential factors, while ΔQ, k and T have their common meanings, as was defined regarding Eq. (2).

When the data are plotted on an Arrhenius-type graph, as in Fig. 3(a) for $P = JE$, in which case the originally exponential increase in current with increasing temperature is theoretically linearized, the important observation is that there is still an unexpectedly steep current (and, then, P) peak manifesting in place of what should have been a mere change in the slope of the straight line (before flash). This presupposes that an additional contributing effect must be considered. Notably, the A → R transformation in titania is reconstructive in nature, which means that it involves the breaking and reforming of the chemical bonds determining the crystal's structure [31,37]. The occurrence of the current peak in Fig. 3(a) is reasonably indicative that bond breaking in the anatase phase impacts the density of ionic charge carriers (N in $J = Nq\mu E$) momentarily free (unbound) and then available to participate in the electrical transport process promoted by the applied field (E), that is, until bond reforming gives rise to rutile.

The phase evolution reported thus far for this titania nanopowder is summarized in Table 3 and specified in Fig. 3(b), including an indication of the region of current peak incidence (hatched area) situated between $T \cong$ 700 and 870 °C, according to curves 1 and 2 in Fig. 2(a). The occurrence of this peak denotes a different dynamic for the entire sintering process at low fields, in which case ignition and the development of a flash are ultimately retarded. Irrespective of this attribute, all these samples were flashed until they reached J_{max} = 50 mA·mm^{-2} (with holding time of t_{flash} = 120 s at J_{max}), resulting in highly dense materials. We have included in Table 2 the final (average) values of material density, that is, relative to the theoretical value corresponding to rutile (ρ_R^{theo} = 4.24 g·cm^{-3}). In particular, the one-step (A + R) → (R+ high densification) scenario, i.e., synthesis plus consolidation registered at flash, applying $E \geq$ 300 V·cm^{-1}, constitutes what can be considered a reactive flash sintering situation. Figure 3(b), which shows phase development with changes in processing temperature, applied electric field (E), and T_{furn}^{flash}, represents a phase diagram for this material and may serve as reference data for other works.

For comparison with the literature, the flash onset temperature values from Ref. [6] have also been included in Fig. 3(b) using closed symbols. These denote where a single rutile-structured TiO_2 powder (with a similar starting particle size) would flash depending on the magnitude of the applied field. The data are comparable for high fields, e.g., E = 500 V·cm^{-1} led to T_{furn}^{flash} = 700 °C [6] vs. 705 °C (average value) in this work. To account for this coincidence, we must remember (see discussion above) that, for $E \geq$300 V·cm^{-1}, the (A + R) → R phase transition occurs at

Table 2 Applied field (E) and resulting values of furnace temperature at flash (T_{furn}^{flash}), relative density (ρ_{rel}), and average grain size (AGS) processed for flash experiments conducted on TiO_2-P25. These values were averaged from 3 to 4 experiments. Maximum current density preset to flow across sample was J_{max} = 50 mA·mm^{-2}. Values of ρ_{rel} and AGS correspond to samples with holding time of t_{flash} = 120 s at J_{max} (toward the steady-like state)

E (V·cm^{-1})	T_{furn}^{flash} (°C)	ρ_{rel} (% TD)	AGS (μm)
150	993	92.9	0.48
200	947	93.2	0.43
300	755	93.1	0.24
400	732	93.2	0.18
500	705	94.6	0.19

Table 3 Phase development in A plus R polymorph-containing titania (TiO_2-P25) nanopowder when subjected to electric field-assisted thermal processing

E (V·cm^{-1})	Temperature → Phases		
	Initial	Intermed#	Final*
150	A + R	R	R
200	A + R	R	R
300	A + R	—	R
400	A + R	—	R
500	A + R	—	R

Note: #before flash; *after flash.

flash or during flash incubation or ignition, a scenario that boils down to having, still at relatively low temperatures, rutile as the starting titania powder, as in Ref. [6].

The above similarity in flash onset temperatures becomes frustrated when the incidence of the aforementioned current peak preceded the flash event, which resulted in a delay to significantly higher temperatures: we found T_{furn}^{flash} = 993 °C at, e.g., E = 150 V·cm^{-1} vs. just 840 °C in Ref. [6], i.e., an appreciable thermal retard of ΔT = 153 °C. In any case, the present results indicate, for example, that there is, in principle, no need for a previous, separate heat treatment (calcination-like step) to first convert anatase to rutile if the final goal is to produce high-density rutile ceramics from anatase raw material. In such a case, flash sintering is an energy-saving and, hence, cost-efficient solution, as it is a one-step sintering approach that also allows rapid consolidation at relatively lower furnace temperatures.

Figures 6(a) and 6(b) show representative SEM micrographs (cross section) of the titania samples after flash sintering at E = 200 and 500 V·cm^{-1}, respectively, with J_{max} = 50 mA·mm^{-2} and t_{flash} = 120 s at J_{max}. Dense microstructures are observed, confirming the high-density values that were measured for these samples (Table 2). The SEM analysis included estimating the average grain size (AGS), and this was done by applying the linear intercept method, as described elsewhere [38]. Figure 7 shows how the AGS ultimately changed with the variation in the applied field, the values of which are also included in Table 2, falling within the 0.2–0.5 μm range. The main observation to highlight is that grain growth is inhibited with increasing E, which is consistent with the tendency generally observed in the literature, as in Refs. [5,6,11,13,16]. This apparent AGS-electric field association is further discussed later in this report. For reference, conventional sintering at 1100 °C/2 min yielded ceramic bodies with AGS ≈ 0.9 μm.

In this work, we were also interested in exploring the effects of the current density preset at flash (J_{max}) on phase development as well as microstructure characteristics, including material densification. Such a systematic study was considered for sintering conducted under E = 500 V·cm^{-1}, with J_{max} = 2.5, 5.0, 10, 20, 30, 40, and 50 mA·mm^{-2}. As we already stated, points (5)–(8) in Fig. 2(b) represent some of those instances where the experiments were stopped, and then the XRD data were also collected at room temperature. Together, these results are presented in Fig. 8(a) with the 600 °C-XRD pattern that applies at point (1A) as a reference. Early on, at the point (8), corresponding to J_{max} = 2.5 mA·mm^{-2}, the synthesis of a rutile-structured TiO_2 material is already a matter of fact, a result that is then reproduced at higher J_{max} values, as expected. Indeed, traces of anatase could still be detected (but truly at the detection border of the technique) at J_{max} = 2.5 mA·mm^{-2}, point (8), and 5.0 mA·mm^{-2}, point (7), as suggested by the magnification of the XRD patterns shown in Fig. 8(b) toward the 2θ = 23°–35° region. These traces completely vanished with a further increase in the current density. These results reasonably suggest that flash incubation, which is responsible for triggering the nonlinear regime, also promotes a significantly increased rate of structural changes (phase development) in this biphasic titania during thermal processing under field action.

Figures 9(a) and 9(b) shows representative SEM micrographs

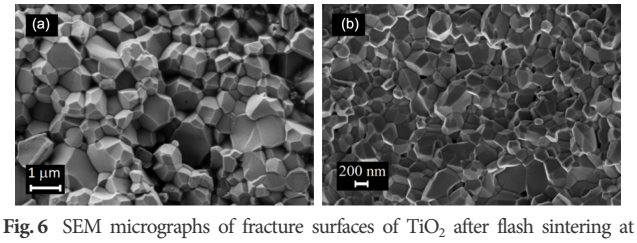

Fig. 6 SEM micrographs of fracture surfaces of TiO_2 after flash sintering at (a) E = 200 V·cm^{-1} and (b) E = 500 V·cm^{-1}, with J_{max} = 50 mA·mm^{-2} and a holding time of t_{flash} = 120 s at J_{max} in both cases.

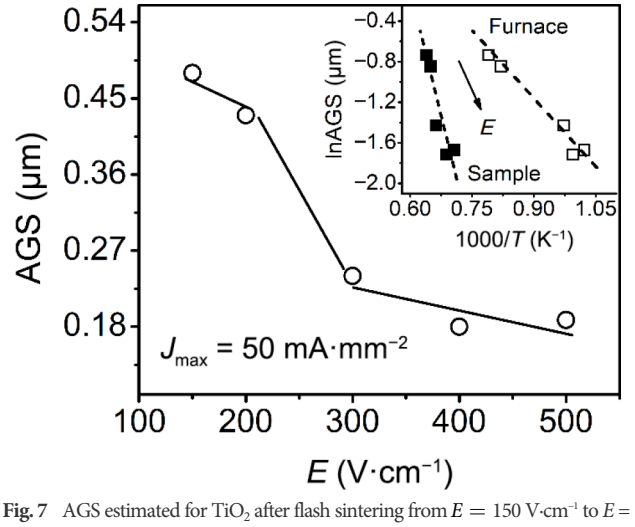

Fig. 7 AGS estimated for TiO_2 after flash sintering from E = 150 V·cm^{-1} to E = 500 V·cm^{-1}, with J_{max} = 50 mA·mm^{-2} and a holding time of t_{flash} = 120 s at J_{max}. Inset is an Arrhenius-type graph showing correlation found between AGS and either furnace or sample sintering temperature at flash. Direction of increasing field E in both sets of data is indicated.

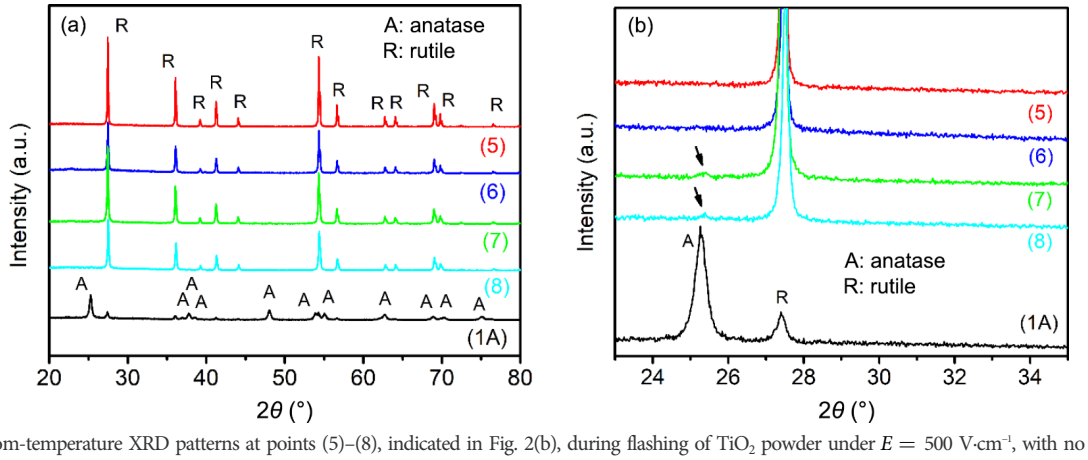

Fig. 8 (a) Room-temperature XRD patterns at points (5)–(8), indicated in Fig. 2(b), during flashing of TiO_2 powder under E = 500 V·cm^{-1}, with no holding time (t_{flash} = 0 s) at all these selected J_{max} values. Pattern at point (1A) has been included as a reference. (b) Magnification of XRD patterns in 2θ = 23°–35° region.

(cross section) of the samples after flash sintering at $E =$ 500 V·cm^{-1} and $t_{flash} =$ 120 s at J_{max}, with J_{max} preset to 40 and 5.0 mA·mm^{-2}, respectively. There was a clear trend for the grains to remain smaller (lower AGS) with decreasing J_{max}: the values were, for example, 0.19 μm at 50 mA·mm^{-2} (Fig. 6(b)), 0.12 μm at 40 mA·mm^{-2} (Fig. 9(a)), and 0.08 μm at 5.0 mA·mm^{-2} (Fig. 9(b)). Figure 10 shows the values of material density achieved immediately after J_{max} was reached, i.e., $t_{flash} \approx 0$ s, and after $t_{flash} =$ 120 s. The density increases with increasing J_{max} and holding time at J_{max}. Accordingly, a time period of 120 s is long enough to produce high-density materials ($\geq$ 92% TD) when the current density $J_{max} \geq$ 10 mA·mm^{-2}, i.e., with no need to impose J_{max} values as high as 50 mA·mm^{-2}. Similarly, high material densities were also achieved in Ref. [6] for rutile powder flash sintered at a relatively low current density of $J_{max} =$ 12 mA·mm^{-2}.

Providing a list of ingredients that contribute to the ignition of flash sintering in materials is still a matter of debate. Nevertheless, the flash phenomenon has been shown to have some apparent connection with a critical-like power dissipation density ($P \approx$ 7–50 mW·mm^{-3}) to reach across the sintering body [39,40]. The critical values found in this work fell within this range, as highlighted in Fig. 3(a). They appear to approach 70 to 80 mW·mm^{-3}, for $E =$150 and 200 V·cm^{-1}, perhaps only because of (relative) proximity of the flash event to the manifestation of the preflash power dissipation peak: a kind of overlap effect. The sample (T_{sample}) and furnace (T_{furn}) temperatures in flash experiments satisfy $T_{sample} = T_{furn} + \Delta T_{Joule}$, implying that $T_{sample} \geq T_{furn}$ at any furnace temperature, where $\Delta T_{Joule} = f(P)$ refers to the contribution from Joule heating. The approximate (upper bound) value of T_{sample} can be estimated from the black-body radiation model [41] according to Eq. (3):

$$\frac{T_{sample}}{T_{furn}} = \left[1 + \frac{P}{e_m \sigma_{SB} T_{furn}^4}\left(\frac{V}{A}\right)\right]^{1/4} \quad (3)$$

where P is the power dissipation density, V/A is the sample volume (V) to the surface area (A) ratio, $\sigma_{SB} = 5.67 \times 10^{-8} \mathrm{W \cdot m^{-2} \cdot K^{-4}}$ is the Stefan–Boltzmann constant, T is the absolute temperature, and e_m is the emissivity, which can be reasonably taken as unity for oxides [6,41]. The values of T_{sample} estimated for sintering under $E =$ 500 V·cm^{-1} toward, for example, the $J_{max} =$ 10–50 mA·mm^{-2} current region of higher sample densification (Fig. 10) ranged from 967 to 1142 °C vs. flash onset at a furnace temperature of 705 °C (on average). This means that the condition $T_{sample} \gg T_{furn}$ applies during flash as long as J_{max} is preset to a value sensibly high [16,41–43]. Such a scenario is expected to cause enhanced mass transport and material densification as well as grain growth with increasing J_{max}, as is reported here and has also been reported elsewhere [3,11].

According to the data shown in Fig. 7, a marked decrease in the AGS is observed from $E =$ 200 to $E =$ 300 V·cm^{-1}, which is in line with the similar behavior observed for T_{furn}^{flash}, as shown in Fig. 3(a). This finding suggested that a direct correlation between the AGS and temperature should naturally exist. This is the result depicted in the inset of Fig. 7, where the AGS-temperature dependence ($J_{max} =$ 50 mA·mm^{-2}) is shown via an Arrhenius-type graph. Linear data behavior is observed, irrespective of whether the sample (closed symbols) or even the furnace temperature (open symbols) at flash is considered, allowing us to conclude that the changes observed for AGS, when the applied electric field is varied, are indeed directly linked (cause–effect relationship) to temperature. It is clear from the literature that several other parameters may influence the flash onset temperature, such as the starting particle or grain size, density of defects, intrinsic conductivity, and reduced atmosphere [2,34,44]. Notably, here, we are exclusively concerned with the effect of the applied electric field (i.e., keeping the other parameters unchanged).

Importantly, the grain growth processes in dissimilar ceramic systems during isothermal annealing can be analyzed via Eq. (4) [45–47]:

$$D^n = K \cdot t = K_o \cdot t \cdot \exp\left(-\frac{\Delta H}{RT}\right) \quad (4)$$

where D is the instantaneous AGS, n is the grain growth exponent, t is the holding time ($t_{flash} =$ 120 s in this work), K is a constant that depends on material properties (including factors like grain-boundary energy and mobility) and temperature, $R =$ 8.31 J·mol^{-1}·K^{-1} is the ideal gas constant, and K_o, ΔH, and T have common meanings. Here, we analyzed the AGS data from the same holding time (and the same preset current density: $J_{max} =$ 50 mA·mm^{-2}), as the flash sintering temperature varied with changing electric field.

Equation (4) is valid when $D \gg D_o$, where D_o is the starting average grain size. We here find that AGS = 0.08 μm at $J_{max} =$ 5.0 mA·mm^{-2}; thus, $D_o <$ 0.08 μm, that is, well below (we can imagine) the AGS values listed in Table 2. According to this equation, the activation energy can be estimated from the data shown in the inset of Fig. 7 as $\Delta H = nR\varnothing$, where $\varnothing$ is the slope value directly extracted from the linear data behavior. At this point, two observations need to be noted. The nonchanging slope for the AGS data in the inset of Fig. 7 implies a nonchanging value of n (at least, toward the temperature region under analysis), whereas a nonnegligible D_o value would have also caused (this was not the case) a divergence of the AGS data from the linear behavior, that is, toward low temperatures (low AGS values). For $n =$ 2, which is the ideal value for grain-boundary migration during grain growth, the activation energy that we estimated from considering the sample temperature data (closed symbols) is $\Delta H = 252 \pm 30$ kJ·mol^{-1}. This value is comparable with that of 230 kJ·mol^{-1} estimated in Ref. [47] for the thermally activated grain-boundary diffusion mechanism in TiO_2.

A sudden increase in the current density and sample temperature at T_{furn}^{flash}, as registered in this work, is a characteristics (fingerprint) of the flash sintering phenomenon. This has allowed researchers to consider that temperature is the parameter that likely accounts for flash sintering ignition in materials during processing under field action, as proposed elsewhere by alluding to the thermal runaway of Joule heating [48]. Within the framework of this mechanism, it has even been proposed, by considering that $T_{sample} \gg T_{furn}$ during flash, that flash as well as reactive flash sintering phenomena should be accompanied by high-temperature-induced rapid liquid phase-assisted consolidation [49,50]. The finding here of a cause–effect correlation between the AGS and temperature, including a sudden increase in the AGS during flash (ascribed to grain-boundary diffusion), seems to be in line with this thermal runaway mechanism.

Two observations deserve to be made regarding the apparent connection, as mentioned above, between flash ignition and the critical-like power density to be reached during electric field-assisted sintering of materials. First, it should be noted that this reasoning does not apply to the development of the A → R phase transformation that manifests, as shown in Fig. 3(a), as a preflash power density peak relatively prominent. This is because the temperature of a substance is expected to remain essentially unchanged during phase transformations ($T_{ptransf}^{sample} \approx$ constant), whereas the thermal runaway of Joule heating [48] involves, in

contrast, a marked increase in sample temperature in negative temperature coefficient of resistivity (NTCR) materials, such as in semiconductors and dielectrics, when a significant imbalance is established between the rate of power density input, $P_+ = JE$ (when becoming markedly higher), vs. the actual rate of power dissipation (when becoming greatly lower) at a given instant in the course of flash incubation. The latter power density quantity indeed refers to the radiative energy loss (P_-), which can be calculated by applying the black-body radiation model (the inverse approach using Eq. (3)); see details in Ref. [48].

Second, according to Ref. [51], the reconstructive A → R phase transformation, which is exothermic and irreversible in nature (rutile is the thermodynamically stable high-temperature phase of titania), involves a release of heat energy ($\Delta\Omega$) from about -1.76 to $-1.80\ \mathrm{kJ\cdot mol^{-1}}$ (enthalpy values) when it occurs in the 600–900 °C temperature region, toward which estimated heat capacities (C) of $73.10-75.18\ \mathrm{J\cdot mol^{-1}\cdot K^{-1}}$ correspond for rutile. Hence, the potential increase in the sample temperature, i.e., $\Delta T \approx 24$ °C, just at the end of such phase transformation because energy release ($\Delta\Omega = C\cdot\Delta T$) would be relatively negligible, that is, if such energy were hypothetically fully reabsorbed by the end single-phase material, i.e., by rutile as the final transformation product. Such a small ΔT impact on the sample temperature, if occasionally taken into account, would also have made the acceleration of thermal runaway unlikely (see Fig. 3).

The above observation of a sample temperature ($T^{\mathrm{sample}}_{\mathrm{A}\to\mathrm{R}}$) expectedly invariant or nearly so during the phase transformation reinforces the idea that, instead of the mobility ($\mu = \mu(T)$), which increases exponentially with temperature, the development of the preflash peak in Fig. 3(a) is then linked to an increase in the defect density, i.e., N in $P(\equiv JE) = Nq\mu E^2$. This is the scenario we postulated to come into play during the collapse of the chemical bonds in anatase, yielding unbound charge carriers and thus an increase in P, until the structural arrangement ends with the formation of rutile, meaning a rebuilding of chemical bonds and hence a decrease in P, that is, in addition to the abovementioned effect of a reduced free lattice volume compromising charge (ionic) mobility in rutile, compared with anatase.

Finally, in parallel with the thermal runaway approach discussed above, there is also the belief that temperature should not solely account for flash development in materials [40,41,52], and field-induced generation of defects has also been proposed, an argument that seems to also support conclusions drawn from studies applying molecular dynamics [53,54]. Electrochemical (redox) reactions occurring at the electrodes, which are responsible for inducing or improving oxygen vacancy and electronic transport during flash, have also been reported elsewhere [40,52,55]. In other words, according to, e.g., Refs. [4,40,41,48–50,52–55], the mechanisms decisively behind or contributing to flash development in materials still remain open to debate, with thermal runaway appearing to be the consequential process ultimately triggered. In addition to other studies presented in the literature, this work has particularly shown that the dynamics of field-assisted flash sintering of materials can vary not only depending on, for multiphase systems, the chemical reactivity of the mixed phases [14–19,50] or not [20], with percolation-mediated flash sintering included as a potential conduction path mechanism in the latter case, but also on whether polymorphic phase transformations, where it is the case, develop toward the (intermediate) temperatures preceding the flash event during the thermal processing under field input. We believe this is an important observation.

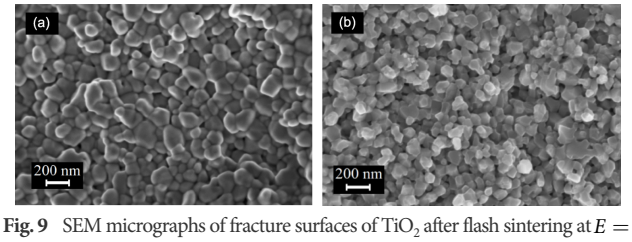

Fig. 9 SEM micrographs of fracture surfaces of TiO_2 after flash sintering at $E = 500\ \mathrm{V\cdot cm^{-1}}$ with (a) $J_{\max} = 40\ \mathrm{mA\cdot mm^{-2}}$ and (b) $J_{\max} = 5.0\ \mathrm{mA\cdot mm^{-2}}$ and holding time ($t_{\mathrm{flash}} = 120$ s) at $J_{\max}$ in both cases.

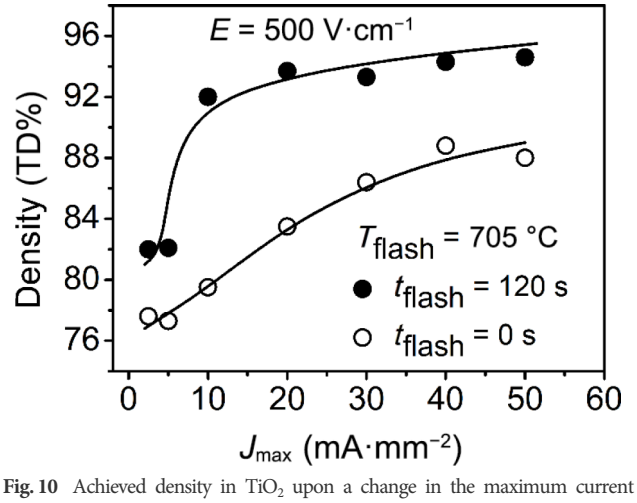

Fig. 10 Achieved density in TiO_2 upon a change in the maximum current density for flash under $E = 500\ \mathrm{V\cdot cm^{-1}}$ at two different instances: just after the preset current density is reached ($t_{\mathrm{flash}} = 0$ s) and after a holding time at $J_{\max}$ ($t_{\mathrm{flash}} = 120$ s).

4 Conclusions

Material evolution during field-assisted sintering of titania containing anatase (A) plus rutile (R) polymorphs was investigated. While high fields promoted flash sintering of the material to progress along with the A → R phase transformation, the scenario was different in low fields, where this transformation preceded toward low temperatures, delaying the flash event to much higher temperatures than expected. In both situations, flash sintering under a suitable predefined current density (as low as $10\ \mathrm{mA\cdot mm^{-2}}$) allowed the production of high-density (≥ 92% TD) titania ceramics in the rutile phase. This work has therefore shown that there is, in principle, no need to consider a calcination-like step to first convert an anatase powder to rutile when aiming for the production of high-quality rutile ceramics as the final product. In that case, flash sintering proved to be a cost-efficient option, as it represents a one-step processing approach that also allows sintering at relatively lower furnace temperatures. Changes in AGS in the flashed bodies were also shown to follow the classical grain growth model, meaning that they remain directly linked to the sample temperature at flash, a parameter that, in turn, is controlled by the magnitude of the applied field. In other words, applied field mediates but does not (directly) determine the AGS, whereas temperature does. This is even more evident when observing that the AGS changed with varying current density ($J_{\max}$), even for an unchanged field. In summary, as expected, at least from power dissipation, both the electric field and current density separately mediated the degree of material densification and AGS through temperature. Therefore, adjusting these processing parameters is the key point in controlling the material properties according to the intended application. The results presented in this report are telling, as they help to understand how

electric field-assisted sintering of materials can unfold when accompanied by phase transformation.

Acknowledgements

This work was supported by the Coordenação de Aperfeiçoamento de Pessoal de Nível Superior-Brazil (CAPES), under Finance Code 001; the Conselho Nacional de Desenvolvimento Científico e Tecnológico-Brazil (CNPq), under grant Nos. 309410/2017-7 and 308474/2021-0; and the Fundação de Amparo à Pesquisa do Estado de São Paulo-Brazil (FAPESP), under grants Nos. 12/06448-0 and 07/54974-5. R.N.R. Silva is also grateful to the Instituto Federal do Tocantins (IFTO) for its support.

Availability of data and materials

The data that support the findings of this study are available from the corresponding author upon reasonable request

Competing interests

The authors have no competing interests to declare that are relevant to the content of this article.

References

[1] Cologna M, Rashkova B, Raj R. Flash sintering of nanograin zirconia in < 5 s at 850 °C. *J Am Ceram Soc* 2010, **93**: 3556–3559.

[2] Francis JSC, Cologna M, Raj R. Particle size effects in flash sintering. *J Eur Ceram Soc* 2012, **32**: 3129–3136.

[3] Francis JSC, Raj R. Influence of the field and the current limit on flash sintering at isothermal furnace temperatures. *J Am Ceram Soc* 2013, **96**: 2754–2758.

[4] M'Peko JC, Francis JSC, Raj R. Impedance spectroscopy and dielectric properties of flash versus conventionally sintered yttria-doped zirconia electroceramics viewed at the microstructural level. *J Am Ceram Soc* 2013, **96**: 3760–3767.

[5] Conrad H, Wang J. Equivalence of AC and DC electric field on retarding grain growth in yttria-stabilized zirconia. *Scripta Mater* 2014, **72**: 33–34.

[6] Jha SK, Raj R. The effect of electric field on sintering and electrical conductivity of titania. *J Am Ceram Soc* 2014, **97**: 527–534.

[7] Zhang YY, Nie JY, Luo J. Effects of phase and doping on flash sintering of TiO_2. *J Ceram Soc Jpn* 2016, **124**: 296–300.

[8] Yang B, Phuah XL, Shang ZX, *et al.* Effects of incubation on microstructure gradient in flash-sintered TiO_2. *Scripta Mater* 2022, **207**: 114270.

[9] Wang QZ, Watts CS, Athanasiou CE, *et al.* The effect of atmosphere on the flash-sintering of nanoscale titania ceramics. *Scripta Mater* 2021, **199**: 113894.

[10] Yoshida H, Sakka Y, Yamamoto T, *et al.* Densification behaviour and microstructural development in undoped yttria prepared by flash-sintering. *J Eur Ceram Soc* 2014, **34**: 991–1000.

[11] M'Peko JC, Francis JSC, Raj R. Field-assisted sintering of undoped $BaTiO_3$: Microstructure evolution and dielectric permittivity. *J Eur Ceram Soc* 2014, **34**: 3655–3660.

[12] Prette ALG, Cologna M, Sglavo V, *et al.* Flash-sintering of Co_2MnO_4 spinel for solid oxide fuel cell applications. *J Power Sources* 2011, **196**: 2061–2065.

[13] Jesus LM, Silva RS, Raj R, *et al.* Electric field-assisted flash sintering of $CaCu_3Ti_4O_{12}$: Microstructure characteristics and dielectric properties. *J Alloys Compd* 2016, **682**: 753–758.

[14] Jesus LM. Conventional, laser and electric field-assisted processing of $ACu_3Ti_4O_{12}$ (A = Ca, $Bi_{2/3}$) electroceramics: (Micro)structure and (di) electrical properties. Ph.D. Thesis. Sao Paulo (Brazil): University of São Paulo, 2016.

[15] Jesus LM, Silva RS, Raj R, *et al.* Electric field-assisted ultrafast synthesis of nanopowders: A novel and cost-efficient approach. *RSC Adv* 2016, **6**: 107208–107213.

[16] Jesus LM, Silva RS, M'Peko JC. Ultrafast synthesis and sintering of materials in a single running experiment approach by using electric fields. *J Adv Ceram* 2019, **8**: 265–277.

[17] Jesus LM, Silva RS, Raj R, *et al.* Electric field-assisted flash sintering of $Bi_{2/3}Cu_3Ti_4O_{12}$ starting from a multi-phase precursor powder. *J Eur Ceram Soc* 2020, **40**: 4004–4009.

[18] Gil-González E, Perejón A, Sánchez-Jiménez PE, *et al.* Control of experimental conditions in reaction flash-sintering of complex stoichiometry ceramics. *Ceram Int* 2020, **46**: 29413–29420.

[19] Wang KW, Ma BS, Li T, *et al.* Fabrication of high-entropy perovskite oxide by reactive flash sintering. *Ceram Int* 2020, **46**: 18358–18361.

[20] M'Peko JC. Flash sintering in well-dispersed insulator-ionic conductor composites: The case of diphasic alumina-zirconia (Al_2O_3-3YSZ) system. *Scripta Mater* 2020, **175**: 38–42.

[21] Rahimi N, Pax RA, Gray EM. Review of functional titanium oxides. I: TiO_2 and its modifications. *Prog Solid State Ch* 2016, **44**: 86–105.

[22] Zhao JZ, Zhang CG, Hu CY, *et al.* Effect of thermal treatment on TiO_2 varistor properties in different atmospheres. *J Eur Ceram Soc* 2017, **37**: 3353–3359.

[23] da Silva LF, Avansi Jr W, Catto AC, *et al.* The role of Nb addition in TiO_2 nanoparticles: Phase transition and photocatalytic properties. *Phys Status Solidi A* 2018, **215**: 1800321.

[24] Ohno T, Sarukawa K, Tokieda K, *et al.* Morphology of a TiO_2 photocatalyst (degussa, P-25) consisting of anatase and rutile crystalline phases. *J Catal* 2001, **203**: 82–86.

[25] Friedmann D, Hakki A, Kim H, *et al.* Heterogeneous photocatalytic organic synthesis: State-of-the-art and future perspectives. *Green Chem* 2016, **18**: 5391–5411.

[26] Koirala R, Pratsinis SE, Baiker A. Synthesis of catalytic materials in flames: Opportunities and challenges. *Chem Soc Rev* 2016, **45**: 3053–3068.

[27] Spurr RA, Myers H. Quantitative analysis of anatase-rutile mixtures with an X-ray diffractometer. *Anal Chem* 1957, **29**: 760–762.

[28] Galizia P, Maizza G, Galassi C. Heating rate dependence of anatase to rutile transformation. *Process Appl Ceram* 2016, **10**: 235–241.

[29] Zhang HZ, Banfield JF. Phase transformation of nanocrystalline anatase-to-rutile *via* combined interface and surface nucleation. *J Mater Res* 2000, **15**: 437–448.

[30] Jiang XZ, Manawan M, Feng T, *et al.* Anatase and rutile in evonik aeroxide P25: Heterojunctioned or individual nanoparticles. *Catal Today* 2018, **300**: 12–17.

[31] Hanaor DAH, Sorrell CC. Review of the anatase to rutile phase transformation. *J Mater Sci* 2011, **46**: 855–874.

[32] Dong YH, Chen IW. Onset criterion for flash sintering. *J Am Ceram Soc* 2015, **98**: 3624–3627.

[33] Jaffe B, Cook WR. *Piezoelectric Ceramics*. New York (USA): Academic Press, 1971.

[34] Chiang YM, Birnie DP, Kingery WD. *Physical Ceramics: Principles for Ceramics and Engineering*. Hoboken (USA): John Wiley & Sons, Inc., 1996.

[35] Nunes LM, Antonelli E, Bernardi MIB, *et al.* How grain boundaries modify the high-temperature dielectric response of ferroelectric electroceramics like $BaTiO_3$. *Mater Res Bull* 2011, **46**: 136–139.

[36] M'Peko JC, Paz FY, Mir M, *et al.* Electromigration and charge carrier density *versus* free lattice volume effects in doped zirconia ceramics. *Phys Status Solidi B* 2004, **241**: 2898–2904.

[37] Penn RL, Banfield JF. Formation of rutile nuclei at anatase (112) twin interfaces and the phase transformation mechanism in nanocrystalline titania. *Am Mineral* 1999, **84**: 871–876.

[38] ASTM. *Standard Test Methods for Determining Average Grain Size Using Semiautomatic and Automatic Image Analysis*. West Conshohocken (USA): ASTM International, 1991.

[39] Raj R. Analysis of the power density at the onset of flash sintering. *J Am Ceram Soc* 2016, **99**: 3226–3232.

[40] Yu M, Grasso S, McKinnon R, *et al.* Review of flash sintering:

Materials, mechanisms and modelling. *Adv Appl Ceram* 2017, **116**: 24–60.
[41] Raj R. Joule heating during flash-sintering. *J Eur Ceram Soc* 2012, **32**: 2293–2301.
[42] Charalambous H, Jha SK, Lay RT, *et al.* Investigation of temperature approximation methods during flash sintering of ZnO. *Ceram Int* 2018, **44**: 6162–6169.
[43] Charalambous H, Jha SK, Phuah XL, *et al. In situ* measurement of temperature and reduction of rutile titania using energy dispersive X-ray diffraction. *J Eur Ceram Soc* 2018, **38**: 5503–5511.
[44] Zhang YY, Luo J. Promoting the flash sintering of ZnO in reduced atmospheres to achieve nearly full densities at furnace temperatures of < 120 °C. *Scripta Mater* 2015, **106**: 26–29.
[45] Lai JKL, Shek CH, Lin GM. Grain growth kinetics of nanocrystalline SnO_2 for long-term isothermal annealing. *Scripta Mater* 2003, **49**: 441–446.
[46] Zhou L, Liu JX, Tu TZ, *et al.* Fast grain growth phenomenon in high-entropy ceramics: A case study in rare-earth hexaaluminates. *J Adv Ceram* 2023, **12**: 111–121.
[47] Höfler HJ, Averback RS. Grain growth in nanocrystalline TiO_2 and its relation to vickers hardness and fracture toughness. *Scripta Metall Mater* 1990, **24**: 2401–2406.
[48] Todd RI, Zapata-Solvas E, Bonilla RS, *et al.* Electrical characteristics of flash sintering: Thermal runaway of joule heating. *J Eur Ceram Soc* 2015, **35**: 1865–1877.
[49] Chaim R. On the kinetics of liquid-assisted densification during flash sintering of ceramic nanoparticles. *Scripta Mater* 2019, **158**: 88–90.
[50] Chaim R, Amouyal Y. Liquid-film assisted mechanism of reactive flash sintering in oxide systems. *Materials* 2019, **12**: 1494.
[51] Smith SJ, Stevens R, Liu S, *et al.* Heat capacities and thermodynamic functions of TiO_2 anatase and rutile: Analysis of phase stability. *Am Mineral* 2009, **94**: 236–243.
[52] Biesuz M, Sglavo VM. Flash sintering of ceramics. *J Eur Ceram Soc* 2019, **39**: 115–143.
[53] Jongmanns M, Raj R, Wolf DE. Generation of Frenkel defects above the Debye temperature by proliferation of phonons near the Brillouin zone edge. *New J Phys* 2018, **20**: 093013.
[54] Xu WW, Maksymenko A, Hasan S, *et al.* Effect of external electric field on diffusivity and flash sintering of 8YSZ: A molecular dynamics study. *Acta Mater* 2021, **206**: 116596.
[55] Biesuz M, Pinter L, Saunders T, *et al.* Investigation of electrochemical, optical and thermal effects during flash sintering of 8YSZ. *Materials* 2018, **11**: 1214.